The Astrophysical Journal, 641:878–890, 2006 April 20

SIMULATING STAR FORMATION AND FEEDBACK IN GALACTIC DISK MODELS

Elizabeth J. Tasker
Oxford University, Astrophysics, Keble Road, Oxford OX1 3RH, UK

and

Greg L. Bryan
Department of Astronomy, Columbia University, New York, NY 10027
Received 2005 August 5; accepted 2005 November 30

ABSTRACT

We use a high-resolution grid-based hydrodynamics method to simulate the multiphase interstellar medium (ISM) in a quiescent Milky Way–sized disk galaxy. The models are global and three-dimensional, and they include a treatment of star formation and feedback. We examine the formation of gravitational instabilities and show that a form of the Toomre instability criterion can successfully predict where star formation will occur. Two common prescriptions for star formation are investigated. The first is based on cosmological simulations and has a relatively low threshold for star formation but also enforces a comparatively low efficiency. The second only permits star formation above a number density of 10^3 cm^{-3} but adopts a high efficiency. We show that both methods can reproduce the observed slope of the relationship between star formation and gas surface density (although at too high a rate for our adopted parameters). A run that includes feedback from Type II supernovae is successful at driving gas out of the plane, most of which falls back onto the disk. This feedback also substantially reduces the star formation rate. Finally, we examine the density and pressure distribution of the ISM and show that there is a rough pressure equilibrium in the disk, but with a wide range of pressures at a given location (and even wider for the case including feedback).

Subject headings: galaxies: evolution — galaxies: ISM — galaxies: spiral — ISM: structure — methods: numerical

Online material: color figures

1. INTRODUCTION

Star formation in galactic disk systems is the product of a large number of physical processes and thus is potentially quite complicated. In outline, gravity tries to form the dense molecular clouds out of which stars form, while rotational shear, thermal pressure, turbulence, magnetic fields, and cosmic-ray pressure resist the collapse. Since the gas in disks does not turn into stars on a free-fall time, one or more of these resistive mechanisms must be effective. The classic condition for disk instability, the Toomre Q parameter (Toomre 1964), encodes the impact of shear, which suppresses large-scale perturbations, and the effective sound speed, or pressure (which suppresses small-scale fluctuation and may be any of the physical processes described earlier). When Q is above some critical value, the large- and small-scale suppression ranges overlap, and no (linear) perturbations are gravitationally unstable.

While this picture is theoretically pleasing and has substantial observational support (Kennicutt 1989; Boissier et al. 2003; Heyer et al. 2004), it is still not perfectly clear which of the physical processes listed above actually supply the local effective pressure. Probably the leading candidate is turbulence because it is seen in all disks and has many of the correct properties, but it should be noted that the magnetic fields and cosmic-ray pressure have similar energy densities (Boulares & Cox 1990). Turbulence in galactic disks can be generated from a number of sources, including gravity (Wada et al. 2002), stellar winds, supernovae (e.g., Mac Low & Klessen 2004), the magnetorotational instability (Sellwood & Balbus 1999), and even radiative heating (Kritsuk & Norman 2002). Whatever the source, the combined effect of the effective pressure, gravity, and shear must reproduce both the observed threshold density for star formation and also the observed relation between gas surface density and star formation (Schmidt 1959; Kennicutt 1989, 1998; Martin & Kennicutt 2001).

A related question is the structure and distribution of gas densities, temperatures, and pressures within the interstellar medium (ISM). Observational and theoretical work have suggested a picture of a multiphase medium with substantial turbulent motions (McKee & Ostriker 1977; McCray & Snow 1979; Larson 1981; Stanimirovic et al. 1999; de Avillez 2000; Elmegreen et al. 2001). However, the distribution of gas (in terms of both volume and density) in the various phases is not well understood, although substantial observational progress has been made (Jenkins 1978; Shelton & Cox 1994; Ferguson et al. 1996; Chu 1999; Shelton et al. 2001). It is clearly important to try to probe this topic theoretically in order to tease apart the connection between star formation, feedback, and the ISM, not simply for a better understanding of our Galaxy and local galaxies, but also to model star formation and galaxy formation at high redshift.

Numerical work often focuses on one of two aspects: either a detailed analysis of the ISM and a smaller simulation area, or a study of the global disk instabilities and star formation at the cost of a simplified ISM model. Models that have tackled both topics have either been in two dimensions (Wada & Norman 2001) or restricted to a box size a few hundred parsecs across (Wada 2001).

Work performed in two dimensions by Rosen & Bregman (1995) allowed the ISM to evolve self-consistently but treated the stars as a collisional rather than collisionless fluid. They modeled the galaxy side-on so that the simulation region included a dimension out of the disk. They found that the gas formed a three-phase medium with cold and warm filaments surrounding bubbles of hot gas. The bubbles of hot gas extend to up to a kiloparsec across, with filamentary structure similar to that observed in our own Galaxy.

Self-consistent treatment of the ISM and star formation has been performed in two dimensions (with both dimensions in the plane) by Wada & Norman (2001) and in three dimensions over a small box size (Wada 2001). They see three phases but also gas that exists in unstable regions between these phases. They therefore argue that a simple two- or three-phase model of the ISM is not sufficient to represent it properly, and that turbulence results in the smearing out of the phases so that gas exists outside pressure equilibrium. Wada also finds that the hot gas is a product of the supernova explosions, and both the hot and warm gas exist off the surface of the disk, leaving the cold gas on the disk plane.

In three dimensions but considering a small section of disk, de Avillez (2000) also utilized a separate stellar disk to explore the collective effects of Type I and II supernovae on the structure of the ISM. His simulations were performed in three dimensions for a section of a galactic arm, located 8.4 kpc from the galactic center using a fixed gravitational field. The supernova locations were determined randomly but with constraints imposed to give a realistic distribution. His results show cold gas is present in a thin, irregular layer on the galactic plane, intercrossed with tunnels of hot gas from supernova explosions. Around the cold gas is a thick disk of neutral warm gas up to 500 pc, followed by ionized warm gas and then hot gas at heights above 1.5 kpc. Places where several supernovae merge form reservoirs of hot gas that have enough energy to break free of the gravitational pull of the stellar disk and expand upward in large bubbles.

Korpi et al. (1999) modeled a section of the ISM self-consistently, including the effects of Type I and II supernovae and that of magnetic fields, but left out star formation and self-gravity. Their ISM formed a two-phase structure of warm and hot gas with a bimodal temperature-density distribution. The warm gas was found in scale heights less than 500 pc and the hot gas above that. They also found a cold component, due to compression by the warm gas, which was found at heights of less than 100 pc. The supernovae in their simulations clustered to produce large nonspherical shells.

Several numerical studies have simplified their treatment of the ISM to study the global properties of the disk and star formation. Robertson et al. (2004) and Semelin & Combes (2002) both assumed a two-phase ISM consisting of cold clouds embedded in a warm gas in pressure equilibrium. The ratio of gas in these two phases is controlled statistically by allowing gas to switch phases during supernova explosions, conduction, and cooling processes.

In their paper, Robertson et al. (2004) compared simulations that used first no star formation, then star formation but no feedback, and finally feedback with a two-phase ISM. In the nonfeedback cases, the gas cooled extremely efficiently, resulting in a nearly isothermal ISM. They found that in these cases, disk fragmentation was catastrophic and the stars (when present) ended up in two big clumps. The addition of star formation stabilized the disk for slightly longer than that in the no–star formation case. In both cases, the fragmentation was due to the Toomre instability (Toomre 1964). The addition of feedback and a multiphase ISM resulted in increased pressure support and a smoother distribution of gas and stars.

Li et al. (2005a, 2005b) used an isothermal gas for the ISM and examined star formation for two different temperatures. They found in both cases the gradient of the gas surface density plotted against the surface density of the star formation rate is around 1.5, in good agreement with the Schmidt law and the observations of Kennicutt (1989). They also observed a threshold for star formation, where no stars are formed past two radial scale lengths. This is also the point at which the Toomre Q parameter drops below 1 and the disk becomes stable to Toomre instabilities.

Kravtsov (2003) performed hydrodynamic simulations in a cosmological context. In this work, the gas is converted into stars on a characteristic gas consumption timescale, rather than on the dynamical time. Kravtsov finds that this can still reproduce the Schmidt law with a gradient of 1.4. The addition of feedback in these simulations results in considerably more hot gas at low densities, although the probability density function of the gas density remains unchanged.

This paper is the first step in a longer range plan to understand the fundamental processes of star formation and feedback in a galaxy disk. These are the first three-dimensional simulations of a global disk without the need to simplify the structure of the ISM, using a grid-based code that is better able to resolve the multiphase medium (except for the small-disk simulations of Wada [2001], which are also grid-based). We use this model to investigate local star formation throughout the evolution of the disk, from the early fragmentation of the gas into stars through to the global and local properties of the star formation rate and the effect on the evolution of the interstellar medium. We compare the results for two different models of star formation and with and without the inclusion of stellar feedback from Type II supernovae. Ultimately, we hope the better understanding of star formation gained from looking at our isolated disk will act as a guide to cosmological simulations of galaxy formation. For these simulations we use a high-resolution adaptive mesh refinement (AMR) code, which includes a more sophisticated treatment of star formation and feedback, as well as a full treatment of self-gravity of the gas rather than the fixed potential that is often used. We concentrate on hydrodynamical effects, ignoring (for the moment) magnetic fields and cosmic-ray pressure.

In § 2, we describe our computational approach, and in § 3 we discuss the structural properties of the disk simulations, including the formation of instabilities and the vertical distribution. In § 4, we discuss how star formation is related to the surface density and compare this to observations, while § 5 contains an analysis of the multiphase structure of the resulting ISM.

2. COMPUTATIONAL METHODS

2.1. *The Code*

To model the galaxy disk, we used the structured AMR grid code, Enzo, described in Bryan & Norman (1997), Bryan (1999), Norman & Bryan (1999), Bryan et al. (2001), and O'Shea et al. (2004). Enzo is a three-dimensional hydrodynamics code that uses a grid-based scheme for the gas and particles for the stars. A large advantage to using AMR codes over static grids is that individual regions of the simulation box can have different levels of refinement. This significantly reduces computational time by only refining areas that need it. An AMR code works by initially placing a single, uniform grid over the whole simulation box. This is the "parent" or root grid and consists of large grid squares allowing a small number to cover the entire volume. The small number of grid cells allows the average properties of each cell to be calculated quickly. However, the detail that this grid describes is minimal; anything smaller than one of these cells goes unnoticed. The code therefore looks at each cell and decides whether further resolution is required. In this work, the decision is made based on whether the baryon density is above a threshold value. If it is, a finer "child" grid is placed inside the parent cell, and the properties of each of its grid cells are then computed. The process can then be repeated, with the child grid itself becoming a parent grid and so on until the desired level of resolution is reached. The result

is a nested structure of grids, with very fine grids only over the areas that require high levels of resolution.

The AMR technique has been particularly successful in resolving the multiphase nature of the ISM in the presence of star formation and feedback processes (Slyz et al. 2005). Particle-based codes tend to overmix the hot and cold gas, which leads to an overestimate of the radiative losses, although algorithmic improvements have alleviated this problem somewhat (the problem and proposed solutions are discussed in detail in, e.g., Marri & White [2003] and Springel & Hernquist [2003]). Grid codes suffer less from this problem as the mesh allows distinct boundaries to be more sharply resolved. This is one of the reasons that we use Enzo to study the instabilities produced in the disk and the resulting ISM structure.

The disk is modeled in a three-dimensional periodic box of side 1 h^{-1} Mpc. The size of the parent grid is 128^3, and we proceed down to an additional eight subgrids of refinement, which gives us a maximum resolution (i.e., minimum cell size) of about 50 pc (and include some runs with resolution down to 25 pc). Once set up, the disk was allowed to evolve over a period of $\Delta z = 0.1 \approx 1.4$ Gyr. The simulations were performed using comoving coordinates, although over the small range of redshift examined here, the impact of the expansion is very slight (for completeness we note that the model adopted is a ΛCDM universe with $\Omega_m = 0.3$, $\Omega_\Lambda = 0.7$, and $H_0 = 67$ km s^{-1} Mpc^{-1}).

The gas is evolved using a three-dimensional version of the ZEUS hydrodynamics algorithm (Stone & Norman 1992). Radiative gas cooling follows the cooling curve of Sarazin & White (1987) down to temperatures of 10^4 K. Further cooling down to $T_{\rm min} = 300$ K is introduced in the second simulation and used thereafter, where the cooling curve is extended using rates given in Rosen & Bregman (1995). This is larger than the minimum temperature of dense molecular clouds but is in the upper range of temperature for the cold neutral medium (Wolfire et al. 2003). In their paper, Rosen & Bregman (1995) argue that other physical processes (e.g., cosmic-ray pressure or magnetic fields) may be crudely modeled by such a choice. More practically, it allows us to observe the formation of a multiphase medium, including the primary phases commonly discussed, and yet resolve the Jeans length over most of the disk (we will return to this issue in more detail).

For the simulations in which star formation was allowed to occur, the following criteria were used to decide whether a grid cell would produce a star (Cen & Ostriker 1992; O'Shea et al. 2004): (1) the gas density in that grid cell exceeds a threshold density, (2) the mass of gas in the cell exceeds the local Jeans mass, (3) there is convergent flow (i.e., $\nabla \cdot \boldsymbol{v} < 0$), and (4) the cooling time is less than the dynamical ($\tau_{\rm cool} < \tau_{\rm dyn}$), or the gas temperature is at the minimum allowed value. If a grid cell meets all the previous criteria, then some gas is converted into a "star particle." The mass of this star particle is calculated as

$$m_* = \epsilon \frac{\Delta t}{t_{\rm dyn}} \rho_{\rm gas} \Delta x^3, \tag{1}$$

where ϵ is the star formation efficiency (more properly the efficiency per dynamical time), Δt is the size of the time step, $t_{\rm dyn}$ is the time for dynamical collapse, and $\rho_{\rm gas}$ is the gas density. This set of conditions has one extra criterion added to it: even if a cell fulfills all of the previous four criteria, a star particle will not be formed if its mass is less than a minimum star particle mass $m_{*\rm min}$. In most of our simulations, the value for $m_{*\rm min}$ used was 10^5 $M_\odot$. The reason for this addition is purely computational: a large number of small stars would greatly slow down the simulation. However, in the case in which this criteria is the only mechanism preventing a star particle from forming, a bypass exists that allows a star particle with mass less than $m_{*\rm min}$ to form with a probability equal to the ratio of the mass of the predicted star particle over $m_{*\rm min}$ (in which case the resulting star mass is $m_{*\rm min}$ or 80% of the mass in the cell, whichever is smaller).

To model the star formation in a molecular cloud, which will typically spread out over a dynamical time, the star particle's formation is spread out over time such that its mass at a time t is

$$m_{\rm stars}(t) = m_* \int_{t_{\rm SF}}^{t} \frac{(t - t_{\rm SF})}{\tau^2} \exp\frac{-(t - t_{\rm SF})}{\tau}\, dt, \tag{2}$$

where m_* is the mass of the star particle, $t_{\rm SF}$ is the time the star particle was formed, and $\tau = \max(t_{\rm dyn}, 10\ {\rm Myr})$.

The code also allows the inclusion of stellar feedback from Type II supernova explosions. This form of feedback has often been suggested as the main driving force for self-regulated star formation. If this option is switched on in the code (as it is for two of our simulations), then 10^{-5} of the rest-mass energy of generated stars is added to the gas' thermal energy over a time period equal to $t_{\rm dyn}$. This is equivalent to a supernova of 10^{51} ergs for every 55 $M_\odot$ of stars formed. All this energy goes into the cell in which the star particle has been created.

2.2. *Initial Conditions*

Our simulations start with an isothermal gas disk with a temperature of 10^4 K and a density profile given by

$$\rho(r,\ z) = \rho_0 e^{-r/r_0} {\rm sech}^2\left(\frac{1}{2}\frac{z}{z_0}\right). \tag{3}$$

Integrating this expression for the density gives us the total mass $M_{\rm gas}(r) = 8\pi\rho_0 R_0^2 z_0$, where $\rho_0 = 2.36 \times 10^{-20}$ kgm^{-3}, which is based on a total gas mass of 1×10^{10} $M_\odot$. We begin with no preexisting stellar disk. We note that the total disk mass we adopt is low compared to the Milky Way disk, which is roughly 4 times more massive (e.g., Klypin et al. 2002), although below we do include one simulation with a heavier disk. For the scale radius and height we took typical values of $r_0 = 3.5$ kpc and $z_0 = 400$ pc, respectively.

The disk sits in a dark matter profile that takes the form described by Navarro et al. (1997). This produces a dark matter mass at a radius R of

$$M_{\rm DM}(r) = \frac{M_{200}}{f(c)}\left[\ln(1 + x) - \frac{x}{1 + x}\right], \tag{4}$$

where the virial mass $M_{200} = 10^{12}$ $M_\odot$, $x = Rc/r_{200}$, and the concentration parameter $c = 12$. Here $f(c)$ is an expression given by

$$f(c) = \ln(1 + c) - \frac{c}{1 + c}. \tag{5}$$

Adding together the gaseous and dark matter mass components allows us to calculate the initial circular velocity of the disk using $V_{\rm circ}(R) = (GM_{\rm tot}/R)^{1/2}$.

2.3. *Summary of the Performed Runs*

Table 1 presents the simulations we ran, outlining the different parameters used in each run. There are four main groups of simulations: simulation A permitted cooling only down to 10^4 K,

TABLE 1
Simulation Parameters

Parameter	T_{min} (K)	minΔx (pc)	ϵ	n_{thresh} (cm^{-3})	Feedback
A	10^4	50	0	0.02	No
B	$10^{2.5}$	50	0	0.02	No
C	$10^{2.5}$	50	0.05	0.02	No
CHIRES	$10^{2.5}$	25	0.05	0.02	No
CLOWEFF	$10^{2.5}$	50	0.005	0.02	No
CFDBCK	$10^{2.5}$	50	0.05	0.02	Yes
D	$10^{2.5}$	50	0.5	10^3	No
DHIRES	$10^{2.5}$	25	0.5	10^3	No
DFDBCK	$10^{2.5}$	50	0.5	10^3	Yes
DJEANS	$10^{2.5}$	25	0.5	10^3	No
DCONST	$10^{2.5}$	50	0.5	10^3	No

which is the minimum allowed by neutral hydrogen line cooling. Simulation B (and the remainder of the simulations) was allowed to cool down to our lower limit of 300 K. Simulation C included star formation with an efficiency typical of large-scale cosmological simulations (5%). This efficiency is appropriate for the galactic disk as a whole, so we adopted a low-density threshold that allows stars to form even in relatively low-density regions (provided they pass the other criteria). In this picture, we admit that we are not following the formation of all dense clumps and thus use a Schmidt-like law to model the star formation rate. Simulation D, on the other hand, assumes that stars will only form in the giant (molecular) clouds resolved in the simulation, and so we adopt a high efficiency and a high threshold (corresponding approximately to a number density of 10^3 cm^{-3}). In addition to the basic C and D runs, we also perform a number of variants. In each case, we include high-resolution runs (CHIRES and DHIRES) that use a root grid with twice as many cells and thus twice the spatial resolution and 8 times the mass resolution of the standard runs as well as runs that include feedback from Type II supernovae (CFDBCK and DFDBCK). In addition, we examine the impact of reducing the star formation efficiency by a factor of 10 (CLOWEFF) and adding an additional refinement criteria that forces the local Jeans length to be resolved by at least four cells (DJEANS), as suggested by Truelove et al. (1997; at least until we reach the maximum refinement level, or the minimum Δx given in Table 1). We also perform one final simulation (DCONST) where we changed our function for star particle mass as given in equation (1) to depend on a set timescale, rather than on the dynamical time.

3. STRUCTURAL RESULTS

In this section, we investigate how the disk cools and fragments and the impact that star formation has on the three-dimensional structure.

3.1. *Evolution and Structure of the Disk*

In the first simulation performed (simulation A in Table 1, with cooling limited to a minimum temperature of 10^4 K), the disk remained largely uniform with only small fluctuations occurring in the central few kiloparsecs. As we show below, this is consistent with our expectations from the growth of gravitational instabilities. No star formation would have occurred even if we had allowed it.

However, when cooling is allowed down to 300 K (as in runs B, C, and D), the result is quite different. Figure 1 shows the growth of the perturbations over the first 150 Myr. The perturbations start in the center where the dynamical time is the shortest (recalling that $t_{dyn} \sim \rho^{-0.5}$) and spread outward with time. Initially, the perturbation begins as a spiral density wave as the radial direction collapses first. This forms spiral filaments that then fragment in the azimuthal direction. Knots quickly appear and accrete matter along the filament, in a manner reminiscent of cosmological structure formation. Eventually, the filament disappears and neighboring knots start to interact. The interactions lead to mergers but also to high-velocity encounters that can strip material from the knots. Eventually, the entire face of the disk that is prone to instabilities develops these clumps. The presence or absence of star formation in our simulations does not significantly change this picture.

These images are similar in many respects to the two-dimensional simulations presented in Wada & Norman (2001), albeit on a somewhat larger scale. Increasing the dimensionality does not appear to significantly change the early evolution of the clumps. However, examining images of disks in a side-on projection shows that the clumps do make excursions out of the plane during interactions, and the later evolution we see differs significantly from the two-dimensional Wada & Norman results. We discuss the vertical structure in more detail below.

Figure 2 shows the later evolution of run B, with cooling. The projections here show the evolution of the disk pressure (*bottom*) in addition to the gas density (*top*) and temperature (*middle*) for

Fig. 1.—Evolution of the gas density as a function of time for the DHIRES run in the central 21.4 kpc of the run. From left to right, the frames are at 50, 100, and 150 Myr, respectively. The density ranges from 10^{-1} to 10^3 $M_\odot$ pc^{-2}.

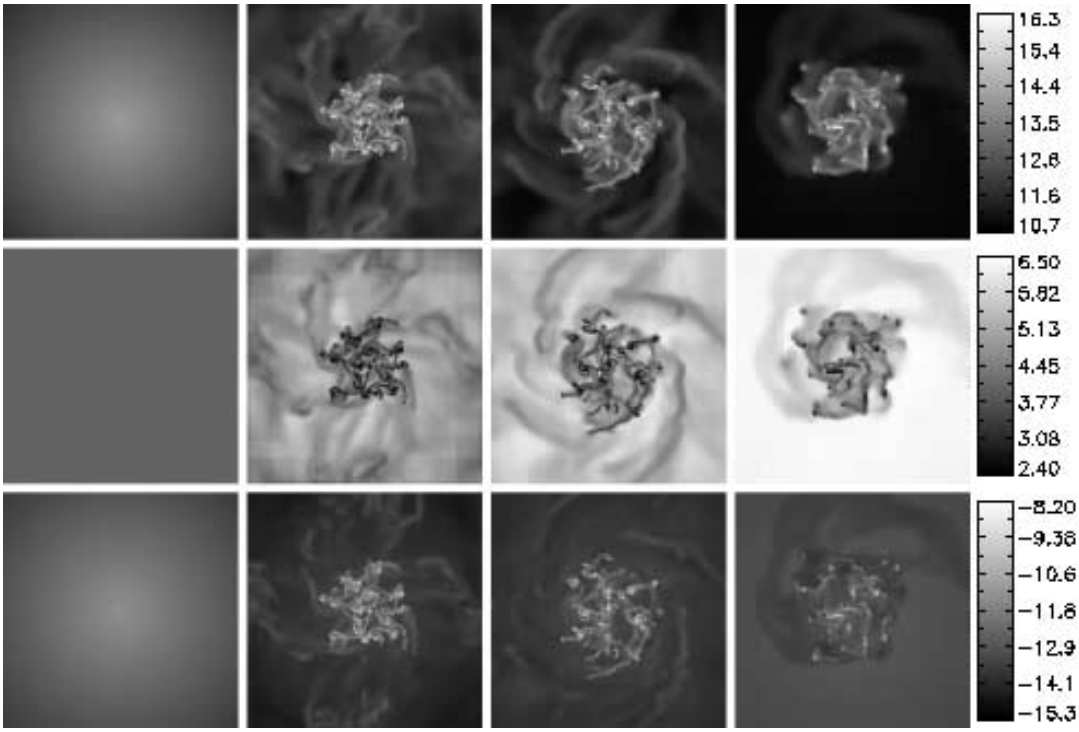

FIG. 2.—Gas surface density (*top*), mean mass-weighted temperature (*middle*), and mean pressure (*bottom*) in the inner 30 kpc region of the simulation box for run B. From left to right, the frames show the results at $t = 0$, 374 Myr, 561 Myr, and 1.32 Gyr. All scales are to the base-10 logarithm, and gas and star particle density is measured in $M_\odot$ Mpc^{-2}, temperatures in K, and pressure on an arbitrary scale. [*See the electronic edition of the Journal for a color version of this figure.*]

four of the simulations outputs. The dense knots show up clearly in the temperature plot as the coldest gas. This is consistent with the very short cooling times implied by such dense gas. Basically, the gas is as cold as our truncated cooling curve allows. The anticorrelation between density and temperature implies some degree of pressure balance. However, the bottom set of panels in this figure show that while this is true for the low- and moderate-density gas, the highest density clumps are significantly overpressured compared to the rest of the ISM (note that the pressure here is only thermal pressure—we do not try to characterize any turbulent component to the pressure). Farther out in the disk (beyond about 10 kpc), the gas fails to form cold, dense clumps. The gas also shocks up to temperatures around 10^5–10^6 K (also the temperature of the gas in the interclump regions near the center of the disk).

In runs C and D, star formation is introduced via the parameters described in the previous section. The initial evolution is quite similar in that the gas quickly fragments, but now the addition of star formation depletes gas from the self-gravitating clumps. Stars only form in the central 10 kpc (where cold clumps exist in Fig. 2). On a timescale of several hundred Myr, the gas is largely converted to stars, and the gas density of the disk drops below that required to sustain instabilities, cutting off star formation except in the innermost regions.

3.2. *Disk Instability*

In Figure 3 we show the gas and stellar densities of the simulations with and without feedback, including a nonfeedback star formation run at high resolution. It is clear that the typical clump size is strongly affected by resolution, with smaller fragments appearing at higher resolution. This is consistent with the fact that we do not always resolve the Jeans length in the center of the disk, particularly for the standard D run. On the other hand, there is a well-defined radius beyond which star formation does not occur, and this does appear to be well resolved. In particular, a run for which we ensure that the Jeans length is resolved (DJEANS) up to the maximum resolution of the adaptive mesh, produces results that are essentially identical. For gas at our minimum temperature (300 K), the Jeans length is 25 pc at a number density of 10^2 cm^{-3}; thus, in the DHIRES run we resolve the Jeans length nearly until the threshold at which gas is converted into stars (10^3 cm^{-3}). Therefore, we believe that the cutoff in star formation beyond a radius of 7 or 8 kpc seen in Figure 3 is a robust result (this low radius compared to the Milky Way is due to our assumed low disk density—a more realistic gas disk would have a larger cutoff radius).

This star formation threshold can be understood with the Toomre stability parameter (Toomre 1964), defined as $Q = \kappa c_s/\pi G\Sigma_g$, where κ is the usual epicyclic frequency, c_s is the thermal sound speed as measured in the disk (about 2 km s^{-1} for our minimum temperature of 300 K), and Σ_g is the gas surface density. This parameter is plotted as a function of radius in Figure 4, along with the current star formation rate (averaged over the last 20 Myr) at that radius for a variety of simulations. In each case, there is a sharp cutoff at a particular value of the Q parameter. From the runs represented in the top panel of Figure 4, we see this cutoff is unaffected by feedback. As we describe below, feedback acts to reduce the star formation rate, but it has no bearing on this stability cutoff point. The critical Q parameter derived this way is about 0.6. A linear analysis for a two-dimensional dimensional disk predicts 1 (Toomre 1964), while a finite disk thickness reduces the critical value to 0.676 (Goldreich & Lyden-Bell 1965; Gammie 2001). We note that Kennicutt (1989) finds values around 1.5; however, we have used the thermal sound speed of the gas rather than the velocity dispersion. If we adopt an effective sound speed of 6 km s^{-1}, this boosts the derived critical value by a factor of 3 and brings it into better agreement with the Kennicutt value.

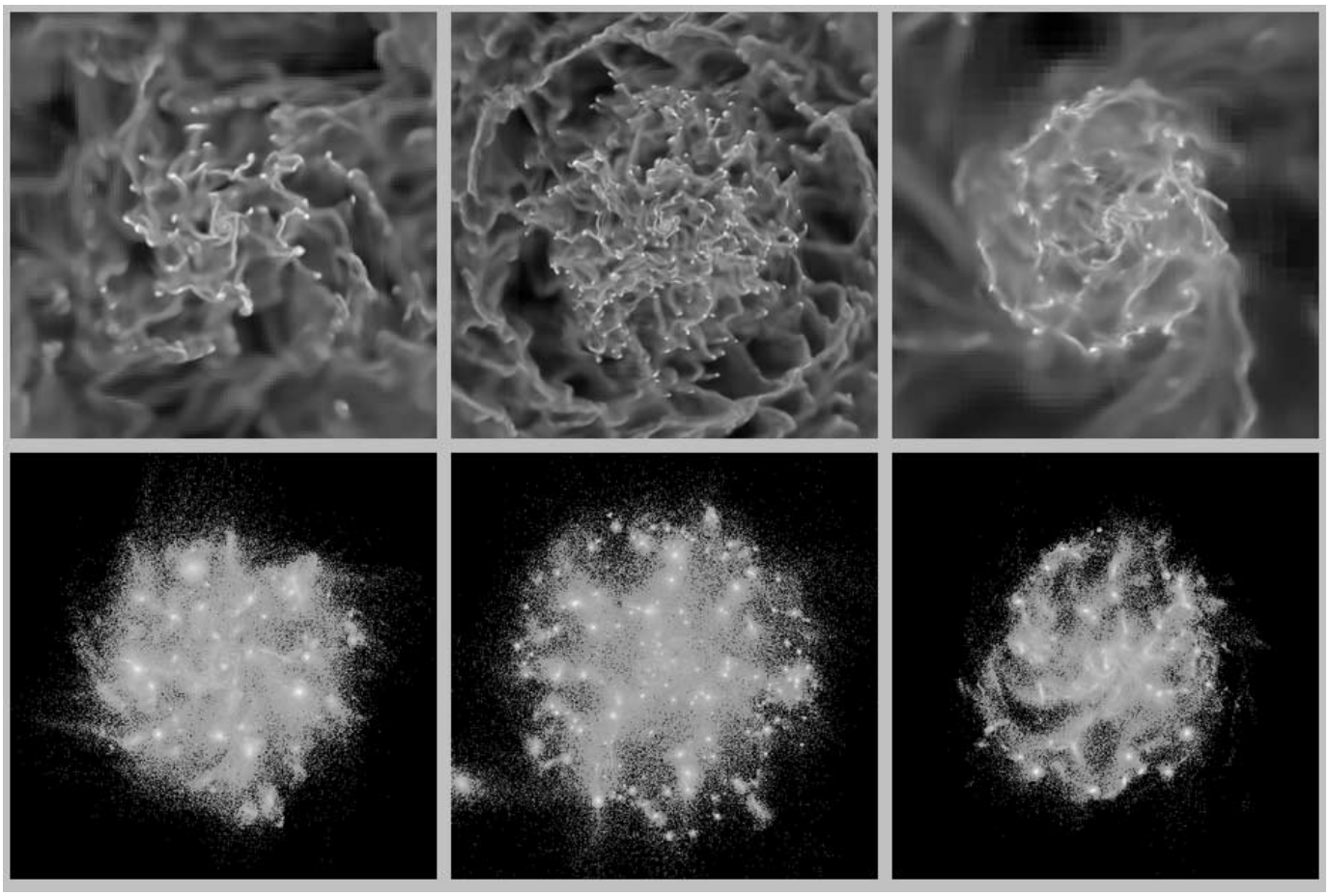

FIG. 3.—Gas density (*top*) and stellar density (*bottom*) in a region 22 kpc on a side after 330 Myr of evolution. The left images are from the simulation with star formation but no feedback, the middle images are from the high-resolution version of this simulation, while the right images are from the feedback simulation.

For comparison, we also calculated the star formation rate and Q for a disk with 4 times the gas mass, which is shown in the bottom panel of Figure 4. The heavier disk draws out the star formation cutoff to a greater radius, in close agreement with the Milky Way's own stellar radius of ~15 kpc. The value for Q at the absolute cutoff for the star formation, $r = 16$ kpc, is 1, slightly higher than that for the original disk. However, the star formation rate starts to decrease at a smaller radius than this, at around $r = 13$ kpc. At this point, $Q \sim 0.5$, a closer agreement to the lighter disk. The Q scaling therefore works well with the changing weight of the disk, especially since the variation of Q over the disk is of order 100. This scaling could be tightened still more with a sharper estimate of the correct position of the star formation rate cutoff.

3.3. *Vertical Scale Height and the Galactic Fountain*

Another important structural property is the vertical scale height. In Figure 5, we show the density profile for the same three simulations discussed previously. Both the low- and high-resolution simulations without feedback show a thin disk, with a scale height of approximately 100 pc. This does not change significantly for the feedback simulation, although there is a clear tail of higher density material that extends about a kiloparsec above and below the disk. This is due to the transient gas streams that are ejected from the disk due to supernova explosions. This scale height is comparable but less than the observed Milky Way H I scale height, which ranges from about 150 pc at a radius of 5 kpc, to 300 pc at the solar radius (Malhotra 1995). Unfortunately, even our highest resolution simulation has a cell size of only 25 pc, so this is, at best, marginally resolved.

This is not to say that the feedback run does not have a substantial impact on the distribution of gas in the plane. Figure 6 shows side-on projections of density, temperature, and pressure for the CFDBCK run. While it is clear from these three plots that most of the gas still lies in the plane, large streamers can be seen reaching several kiloparsecs above and below the plane. Hot bubbles can be seen in the temperature distribution with some gas around 10^6 K, but most are considerably cooler. These bubbles form in the plane but many quickly break out, driving warm, diffuse gas upward. As this gas expands and cools, it is also deaccelerated by halo gas. Clumps of the gas cool and fall back toward the plane. Many of these can be seen at dark spots in the temperature distribution but cannot be seen in the pressure image, indicating that they are in a rough pressure equilibrium with the hotter, more diffuse medium. Although this galactic fountain effect does not significantly change the density profile near the plane, it does very clearly change the dynamics of gas out of the plane. We will examine the observational consequences in a future paper.

4. STAR FORMATION PROPERTIES

Observational studies of star formation indicate that the rate of star formation is closely tied (in a statistical sense) to the surface density of the gas, increasing as $\Sigma_{\rm SFR} \propto \Sigma_{\rm gas}^{1.5}$ (Kennicutt 1989). In this section, we examine how star formation occurs in our model galaxies.

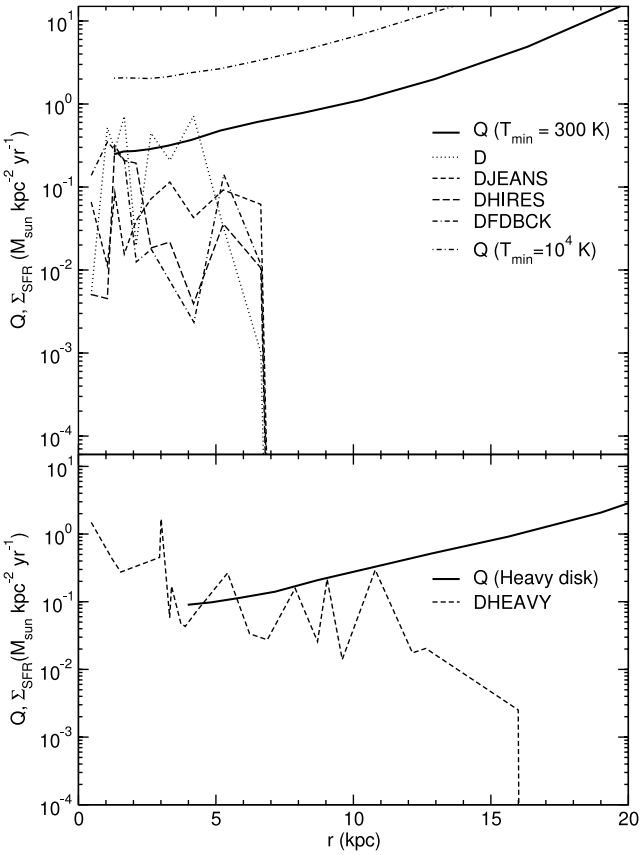

FIG. 4.—*Top*: Solid line shows the Q parameter computed shortly after the start of the D simulation when the gas has reached its minimum value (300 K) but before nonlinear instability formation. The instantaneous rate of star formation (averaged over 20 Myr) is shown for four variants of the D simulation (the C series shows similar results). Note that gravitational instability (and hence star formation) only occurs below a critical Toomre Q parameter. The dot-dashed curve shows the Q parameter for the A simulation ($T_{min} = 10^4$ K), which never falls below this critical value. *Bottom*: Same plot but for a disk with a gas mass 4 times greater than the other simulations. The cutoff this time it at a larger radius and corresponds to a slightly larger Q value.

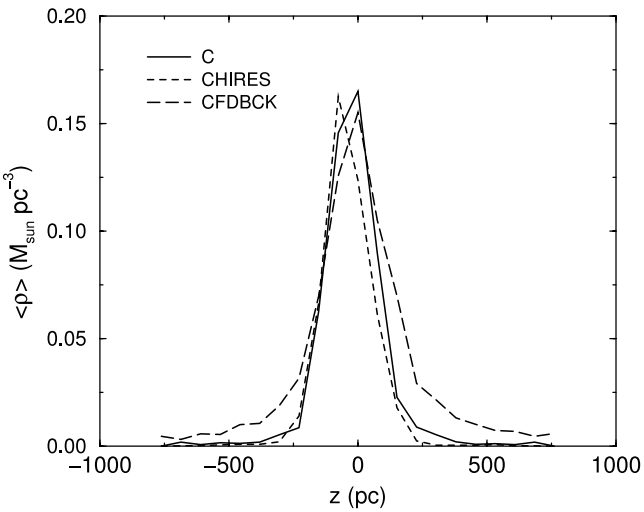

FIG. 5.—Vertical density profile 330 Myr into the evolution for the same three simulations shown in Fig. 3. This is the density profile averaged within 2 radial scale heights.

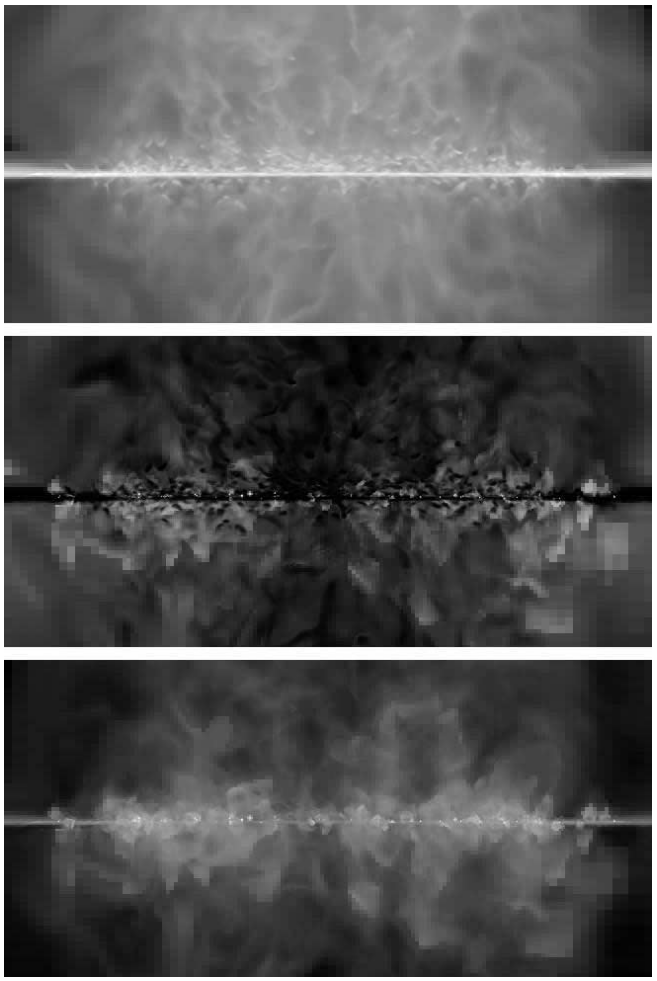

FIG. 6.—Edge-on projections of the CFDBCK run demonstrating the impact of SN feedback (runs without feedback show a thin, cold disk with hot, featureless gas above and below the plane). The top panel shows the projected density, the middle panel shows the mean temperature, while the bottom panel depicts the integrated pressure. Each image is about 22 kpc across and 10 kpc high.

4.1. *Star Formation History*

First, we examine the star formation history in the entire disk as a function of time, as shown in Figure 7. The top panel depicts the results for our model C, both the standard run and the high-resolution CHIRES variant, along with the high-resolution run for the D-algorithm, DHIRES. The close agreement between these curves again demonstrates that the star formation is largely resolved in these simulations. Each curve shows a rapid increase in the star formation rate over roughly 100 Myr, in agreement with the images in Figure 1. The rate then reaches a peak and falls off in an exponential fashion. This is due to the gas depletion resulting from the high star formation rate. After 1 Gyr, nearly all of the gas in the unstable part of the disk is exhausted. This is considerably shorter than the timescale for gas exhaustion in present-day spirals and is related to the higher than observed star formation that we see in these simulations, a point that we return to in the next section.

Remarkably, the star formation history is nearly identical for the D-model for star formation, which is more efficient but limited to the densest parts of the clumps. In fact, this agreement is largely due to our choice of parameters. This is shown clearly in the middle panel of the same figure for the CLOWEFF simulation, which is similar to the C run but with 10 times lower efficiency.

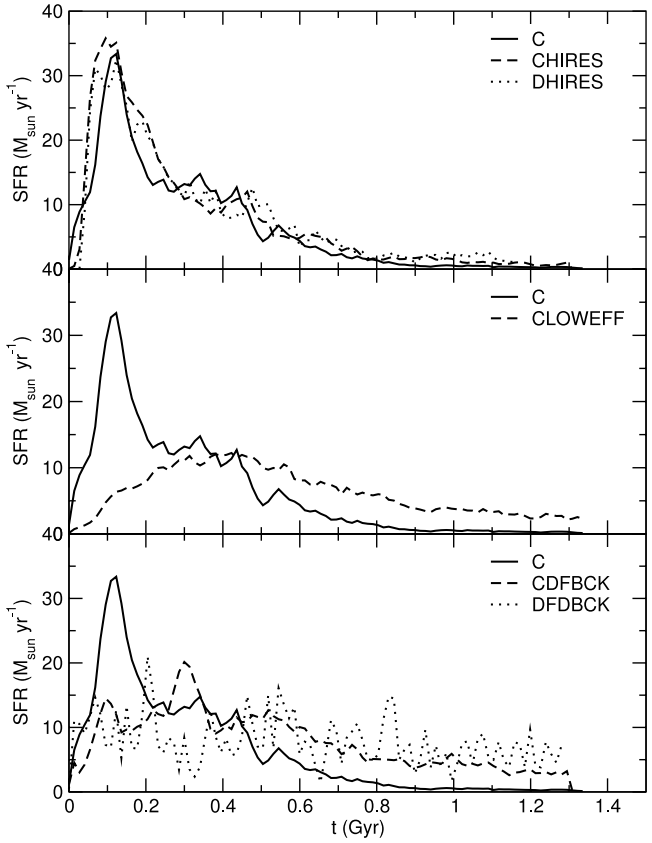

FIG. 7.—Star formation rate as a function of time for the models indicated in the legend.

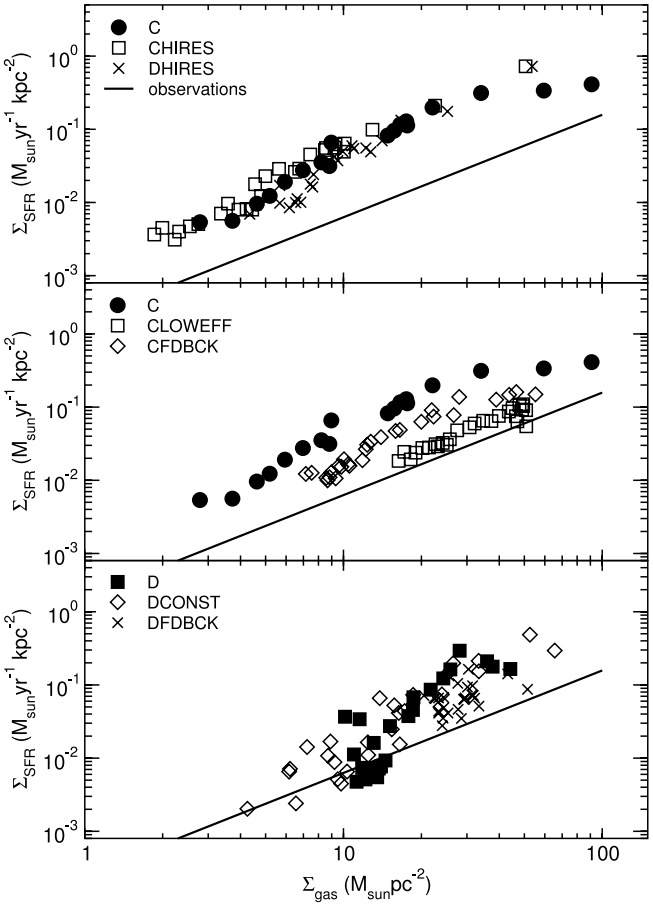

FIG. 8.—Global Schmidt law: Variation over time of the relationship between total star formation rate and gas surface density. Star formation rate is plotted as a function of density averaged over the disk for a variety of models. Each point with the same symbol represents the same simulation at a different time, equally spaced along the 1.4 Gyr simulation run. The solid line is a best fit from observations (Kennicutt 1989).

This lower efficiency run has a much longer timescale for converting gas into stars, with a lower peak rate and more gas left after 1 Gyr. This demonstrates the importance of parameter selection for this type of star formation algorithm (which is very common in cosmological simulations). However, note that the timescale for gas exhaustion is a factor of $\sim$4 longer in the CLOWEFF run than the C run, not the factor of 10 one would expect by decreasing the efficiency by a factor of 10. This occurs because the longer timescale permits larger mass clumps to form (mostly through merging), and the larger clouds generate larger core densities, which increases the star formation rate.

In contrast with the C-type algorithm, the parameter choice (within reasonably bounds) is not important in our D-type run. In a test run with the D-type parameters but with 10 times lower efficiency, the result was nearly identical. This can be readily understood—star formation is only permitted in dense regions where the dynamical time is so short that the gas will be converted into stars in a shorter time than the galactic timescale (the dynamical time for gas at a number density of 10^3 cm^{-3} is about a million years, so even increasing this by a factor of 10 by decreasing the efficiency by 10 would have little effect when compared to the 100 Myr timescales of the disk itself).

Finally, the simulations that include feedback from Type II supernovae with the C-type (CFDBCK) and D-type (DFDBCK) algorithms are shown in the bottom panel. These both show a longer timescale for star formation and, like CHIRES and DHIRES, depict very similar histories. The extended timescale for star formation is in part because individual star-forming clumps are dispersed by the feedback before they can be converted entirely into stars, and in part because winds from star-forming clusters disperse and heat gas in nearby clouds before they can form. The net result is that star formation is (at least partially) self-regulated.

4.2. *Star formation as a Function of Gas Surface Density*

Next, we examine how star formation depends on density, as observations indicate it does. In Figure 8, we show the global star formation rate averaged over the star-forming part of the disk (corresponding to the radius containing 95% of the star formation). The top two panels show results for the same set of simulations as in Figure 7. The C and CHIRES runs are quite similar and run nearly parallel to the observed relation between star formation and surface density, albeit at a rate almost an order of magnitude above that observed. This large star formation is in agreement with the short gas exhaustion times already discussed. Decreasing the efficiency parameter as in the CLOWEFF run produces results that are closer to those observed, although we see again that the decrease in the star formation rate is a factor of 4 rather than the expected order of magnitude decline (we decrease ϵ from 0.05 to 0.005), for the reasons noted earlier. The CFDBCK and DFDBCK run also decreases the star formation rate. In the CFDBCK case this can be seen most clearly to be a factor of 2 reduction for the same star formation efficiency.

One possible reason for the higher than observed star formation rates is related to our inability to model the physics and structure of molecular clouds. Such clouds are observed to form

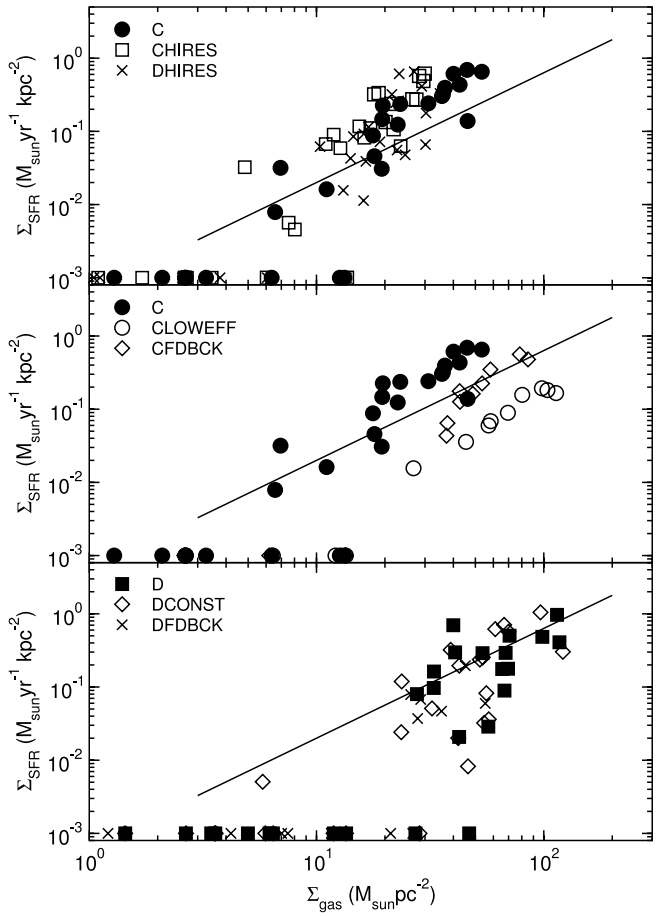

FIG. 9.—Local Schmidt law: Variation over the disk's surface of the relation between star formation rate with gas surface density at a set time, t. Star formation rate is plotted against gas surface density averaged azimuthally in radial bins. Each point (for a given simulation) is averaged over a different radial range but are all from the same point in time approximately 200 Myr after the start of each simulation (other output times follow the same relation). The models shown are the same as in Fig. 8. Radial bins with no star formation at all are shown at the bottom of each graph. The solid line is a curve with slope 1.5, as observations indicate (but with an arbitrary normalization). Note that there is a relatively sharp cutoff for each set of curves below which there is no star formation, in agreement with Fig. 4.

stars with an efficiency that ranges from 5% to 30% (e.g., Lada & Lada 2003), depending on if we are talking about the entire molecular cloud or embedded clusters. The efficiency parameter ϵ is really the star formation efficiency per dynamical time (as an inspection of eq. [1] will confirm), and if a cloud is permitted to evolve for many dynamical time without disruption, then the final fraction of gas converted into stars can be considerably higher (approaching unity). This is true for most of our simulations, since we do not include stellar winds and ionizing radiation, which are thought to be a prime reason for the relatively low efficiency (the exception is for the feedback case in which supernovae can disrupt a cloud after about 10 Myr). Therefore, we should bring down our estimate of the star formation rate by a factor of 3–10 (less for the feedback case).

In Figure 9, we show the relationship between star formation rate and surface density for azimuthally averaged radial bins at a given point in time (unlike the global relation which shows many outputs). Again, the slope is 1.5, in good agreement with observations, showing that the simulation reproduce both the global and local relations (or at least their slopes). Most of the same comments for the top two panels of the previous figure apply to the top two panels of this figure. Note that in the local relations, there is a relatively sharp cutoff at low disk surface densities below which there is no star formation, as discussed in § 3.2.

The slope of the simulated relations in both of these plots is very similar to that observed (although the global relations are marginally steeper, particularly at low disk density rates). For the C simulation series, this is not surprising as this behavior is built into the star formation rate in equation (1) (the dynamical time is proportional to $\rho^{-1/2}$ so $\dot{\rho}_{\rm sfr} \propto \rho^{1.5}$). The D series also uses this relation (but with a higher threshold), and so it appears that here too we have just got out what we put in. However, this is not the case. As discussed earlier, the dense clumps are transformed into stars with a net efficiency that is quite high and largely independent of the parameters chosen. This can be seen in two ways. First, a simulation with an efficiency 10 times lower than the standard D case produced essentially identical results to that shown for the D run. More convincingly, we have performed a run in which we use a constant timescale for formation rather than $t_{\rm dyn}$ in equation (1), which we denote DCONST (the time constant was chosen to be the dynamical time at the fixed threshold density). In this case, the local instantaneous star formation rate is directly proportional to the local gas density; however, the bottom panels of Figures 8 and 9 show a very similar scaling as to the standard D run.

5. PROPERTIES OF THE INTERSTELLAR MEDIUM

Previous theoretical studies (McKee & Ostriker, 1977) have modeled the ISM as a three-phase structure regulated by supernova explosions. This motivates us to divide the simulated gas up into three temperature ranges: The cold ISM with $T < 10^3$ K, warm ISM having $10^3 < T < 10^5$, and the hot ISM, $T > 10^5$ K. The top panels of Figure 10 show the volume of gas in each phase for three of our simulations, while the bottom panels show the same results but for the mass fraction. These have been computed only for gas within 3 radial scale heights and 400 pc above and below the plane in order to focus on gas in the main disk.

The first-order result from these figures is that the volume and mass fractions are generally quite robust to the physical model we use. Generally, most of the volume is taken by the warm and hot phases, with the cold phase occupying a minority of the space in the disk, except during the first few hundred million years of evolution. There are some variations about this picture, of course. In particular, the feedback run (CFDBCK) shows (after about 500 Myr of evolution) a slightly higher volume fraction in the cold phase and a corresponding decrease in the hot phase. The same panel in the mass fraction plots shows that the mass fraction in this phase is relatively unaffected (and quite high), indicating that the material in this cold phase must be less compressed in the feedback run, probably due to supernova-driven cloud disruption.

The relatively large fraction of volume in the hot ISM phase, even for the nonfeedback runs, is somewhat surprising. This gas is heated by the shocks induced via gravitational instabilities that drive noncircular motions, as well as gas falling from above the plane. The mass fraction in this hot phase is extremely small (note that the scale on this panel differs from the others), indicating that this high-temperature material has very low density (and is, in fact, in temperature equilibrium with the other phases).

The mass-weighted phase plots show that most of the mass is in cold, dense clumps (this is particularly true for the CLOWEFF, the low-efficiency case), with the vast majority of the rest in the warm phase. Only a very small fraction of the mass ever gets heated significantly; even for the feedback run (CFDBCK), the mass fraction at temperatures above 10^5 K is always less than 1%.

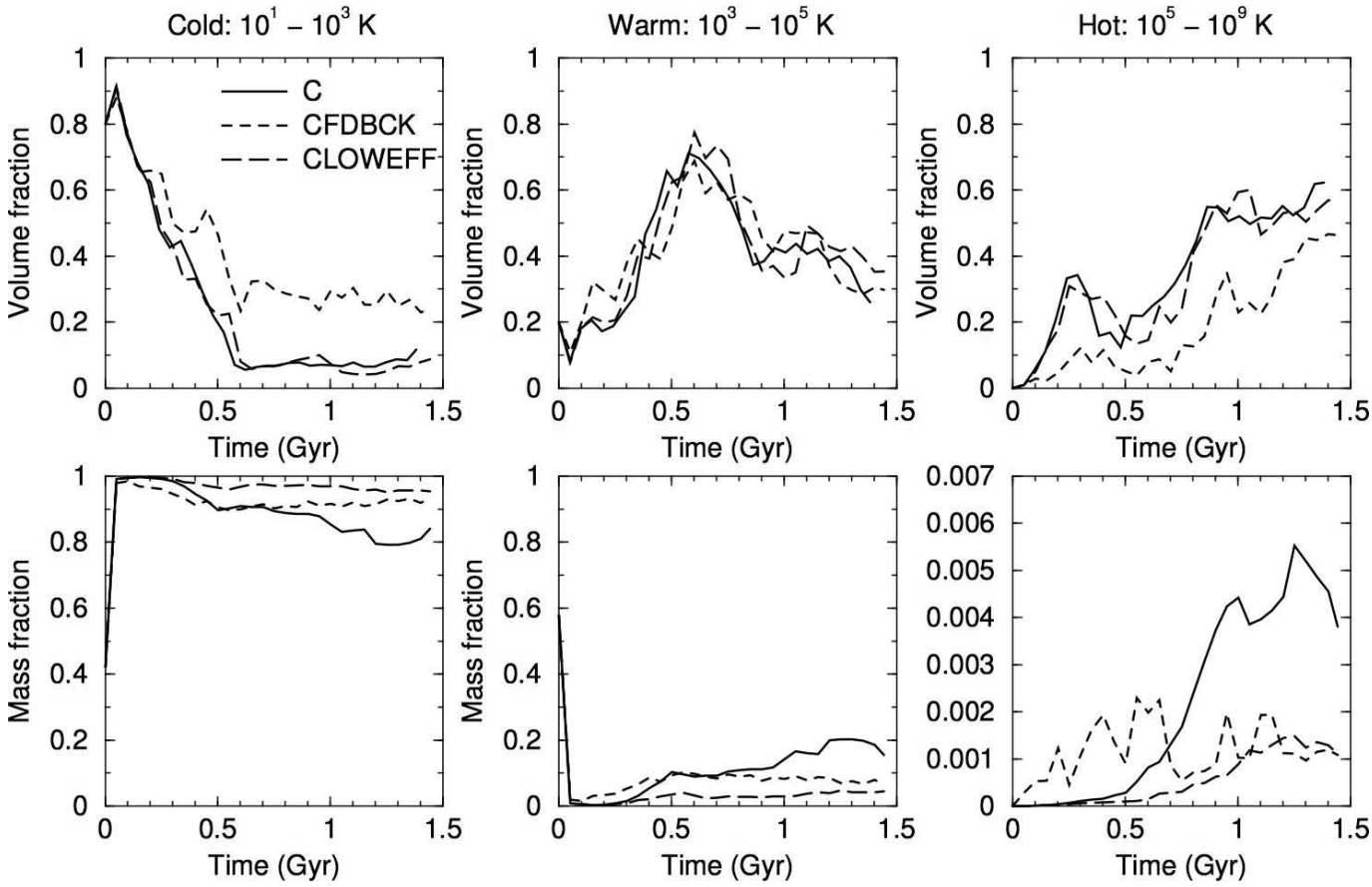

FIG. 10.—Fraction of the ISM volume that is cold ($T < 10^3$ K; *left panels*), warm ($10^3 < T < 10^5$ K; *middle panels*), and hot ($T > 10^5$ K; *right panels*), as a function of time for three simulations. Solid lines represents the standard C run, the dotted line is for the run with feedback (CFDBCK), while the long-dashed lines show the nonfeedback run with a low efficiency of 0.005 (CLOWEFF).

We do not find that feedback increases the hot fraction, which is contrary to many models of feedback in the ISM (e.g., McKee & Ostriker 1977), although the actual fraction of the volume in the hot fraction is in rough agreement with these models. A possible reason for this is that the Type II supernovae we model deposit their energy primarily in dense clumps, leading to their disruption. Although the clumps are unbound by the supernovae, they are not heated to high temperatures and quickly cool back down. This dispersal of dense clouds results in a net increase in the volume occupied by cool clouds for the feedback simulation, as the top right panel shows.

5.1. *Joint Distribution Function*

A simple three-phase model in pressure equilibrium is, of course, an oversimplification. The full nature of the ISM can be better represented in contour plots of density versus temperature for the volume and mass. Figure 11 shows the evolution of the gas volume (*top*) and gas mass (*bottom*) in the C run for the four outputs at $t = 191$ Myr, 567 Myr, 945 Myr, and 1.32 Gyr. The diagonal lines represent lines of constant pressure (assuming an ideal gas equation of state and neglecting ionization changes). The sharp peak on the left-hand side of the plots is due to the cutoff temperature (of 300 K) introduced for radiative cooling.

These contour plots make clear that there is not a sharp division between the three phases discussed earlier, but instead a wide distribution of densities, temperatures, and pressures. However, in all of the diagrams weighted by volume, there are peaks at 10^4 and 10^6–10^7 K, demonstrating that there is some utility in making these divisions. The gas at 10^4 K arises because of the sudden drop in the cooling rate at this point, delaying further gas cooling, while the hotter gas comes from shock heating and is (roughly) the virial temperature of the halo. While there is not an obvious peak at low temperatures in the volume distribution, it is very obvious in the mass distribution, which clearly shows most of the gas residing at the lowest temperature permitted by cooling. We can see that the contour diagrams support the results from the phase diagrams in that the majority of the gas volume is in the hot and warm ISM phases. The mass contour plot shows the vast majority of the mass is in the cool, dense region, and this area shrinks over time as stars are formed from this gas.

By examining the plots along the diagonal direction of constant pressure we can see first that much of the disk is in rough pressure equilibrium, although the width of the distribution perpendicular to these lines show a spread of at least 1 order of magnitude. This indicates that simply the effect of the gravitational instability can generate a substantial range of pressures. There are two regions that clearly do not follow the pressure equilibrium. The most obvious and easiest to explain are the cold, dense clumps that stick up to high densities in a thin line. These are our self-gravitating clouds. We remind readers that the position of this line in the temperature direction is set by the cooling cutoff of 300 K; however, it is clear that even if the gas is simply shifted left by 1.5 orders of magnitude (to the minimum observed ISM temperature of 10 K), it would still be overpressured, even if the density did not increase. The second feature is the peak at 10^4 K, which actually drops below the line

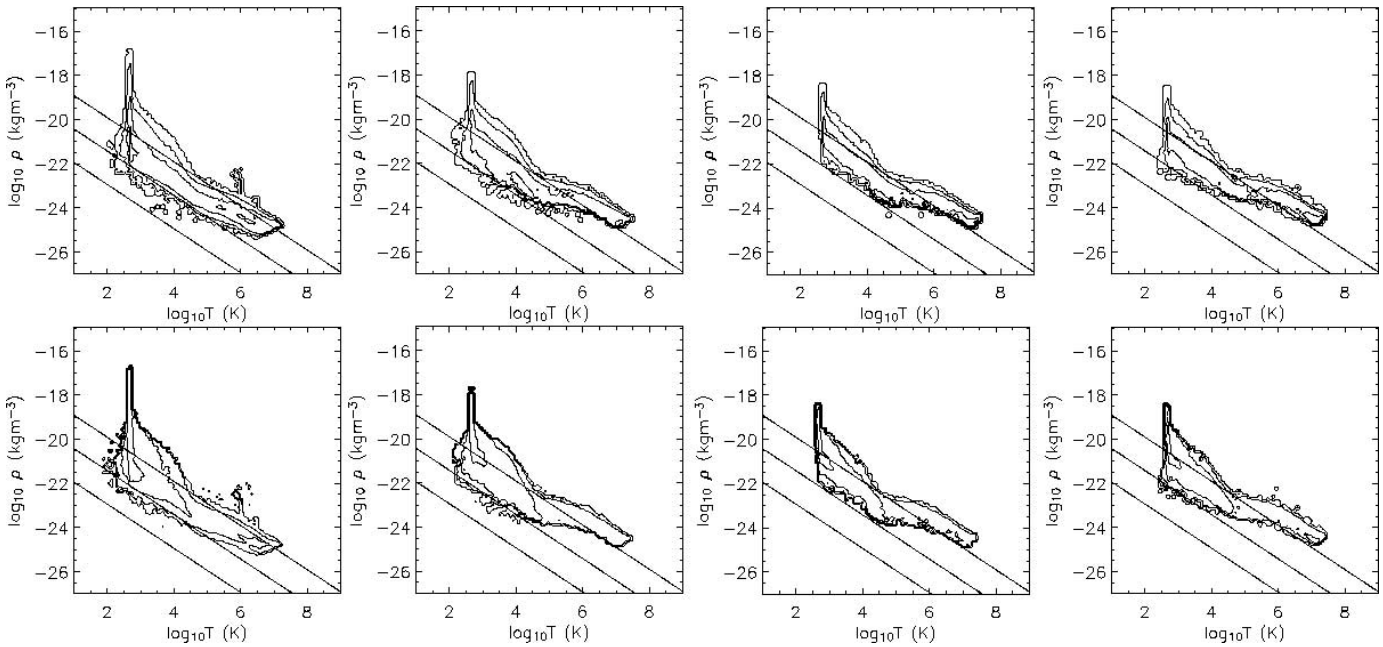

FIG. 11.—Two-dimensional contour plots for the volume (*top*) and mass (*bottom*) in run C with star formation but no feedback. Plots are shown for $t = 191$ Myr, 567 Myr, 945 Myr, and 1.32 Gyr. Diagonal lines represent lines of constant pressure. [*See the electronic edition of the Journal for a color version of this figure.*]

of constant pressure. This probably is a consequence of the thermal instability that sets in around $10^{5.5}$ K, at which point the gas cools so quickly that it drops out of pressure equilibrium with the surrounding gas (e.g., Slyz et al. 2005 and references therein).

The evolution in the distribution function over time is relatively moderate, with a mild increase in the pressure from the first to the second frame (over which period the star formation rate drops significantly), and then constant. This is somewhat surprising considering that most of the gas is converted to stars during this period. However, the mass-weighted distribution makes clear that most of the mass is in the dense, self-gravitating clumps, and it is this mass (which does not contribute significantly to the pressure in the rest of the plane of the disk) that is converted into stars.

Figure 12 shows the distribution functions for the run in which feedback is included (CFDBCK). The most striking feature is the dramatic increase in the width of the distribution function. The injection of supernova energy produces gas with temperatures throughout the full temperature range to be found at a large range of densities. The distribution of pressures is also considerably wider than in the nonfeedback case, although the median pressure at a given temperature does not appear to be significantly

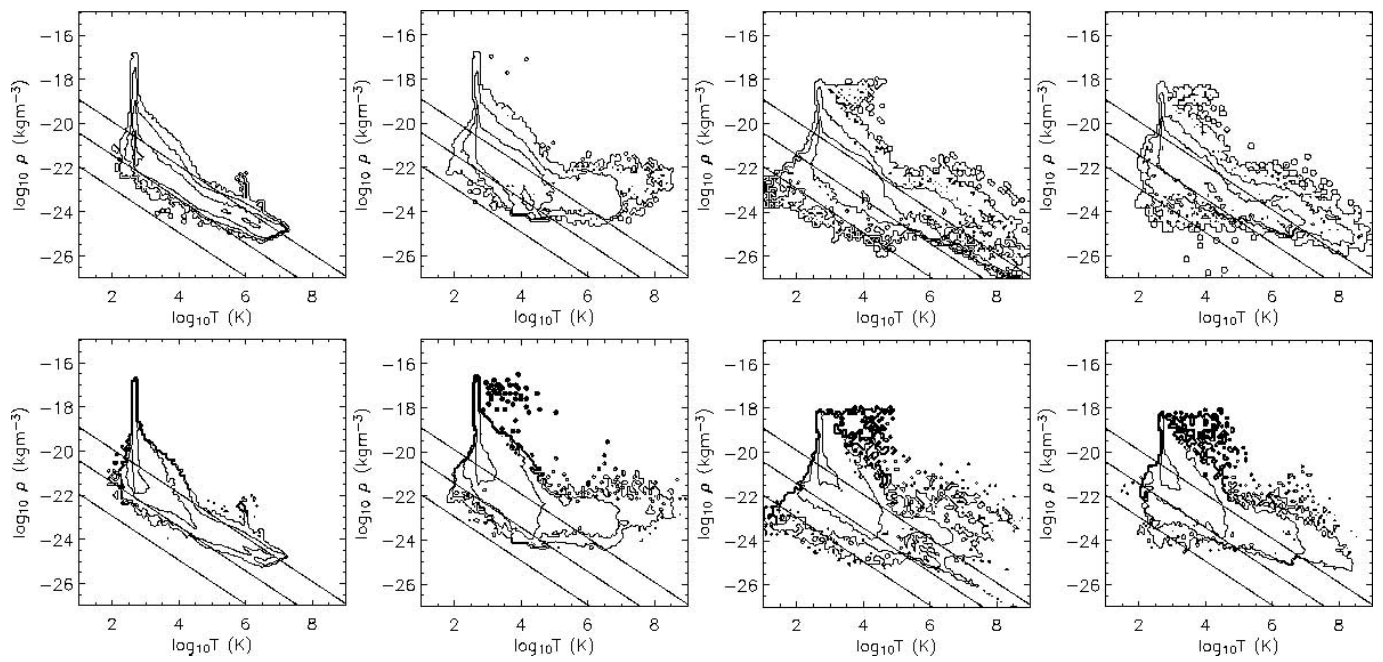

FIG. 12.—Two-dimensional contour plots for the volume (*top*) and mass (*bottom*) in run CFDBCK with star formation and feedback from supernovae. Plots are shown for the same times as the previous figure. [*See the electronic edition of the Journal for a color version of this figure.*]

increased. We also see that the peak in the volume-weighted distribution at high temperatures (and low densities) quickly disperses in the early part of the simulation but starts to reemerge in the final image. The cold, high-density gas on the far left of the contour plots also seems slower to disperse, in agreement with the slower star formation rate documented earlier.

6. DISCUSSION

What controls star formation in our simulations? We break this down into two questions, the first is whether stars can form at all at a given radius in the disk, and second, at what rate? As demonstrated in § 3.2, the growth of instabilities (and hence the possibility of star formation) is clearly controlled via the Toomre instability criteria. We derive a critical Q value of approximately 0.6, in reasonable agreement with a linear analysis of finite-thickness disks (Goldreich & Lyden-Bell 1965) and shearing box simulations (Kim & Ostriker 2001) that find 0.676 and 0.72, respectively. Increasing the disk's gas mass by a factor of 4, in better agreement with a Milky Way–sized galaxy, raises the value of Q to approximately 1, although taking a lower threshold for the star formation cutoff radius gives a Q value of around 0.5. Therefore, Q scales well with the weight of the disk, while refining measurement of the star formation rate cutoff should improve this further. The presence of a stellar disk would modify these results slightly (Kim & Ostriker 2001; Rafikov 2001). The addition of a magnetic field with moderate strength can lead to enhanced collapse due to the magneto-Jeans instability and a larger effective Q value (Kim et al. 2003).

Instabilities result in clouds forming over (roughly) a dynamical period, and so clearly the rate at which gas can be funneled into the densest regions is set by this timescale. In the absence of star formation, the clouds are long-lived entities and continue to accrete gas and grow by mergers (in the B simulation the number of individual clumps drop as the mass of each clump grows until by the end of the simulation only a handful of very large clouds remain). When star formation is turned on, stars form at the highest rate in the dense centers of these clouds, which tend to create bound clusters; this is particularly pronounced in the D series, where star formation is only allowed in the dense cores. As long as there is no feedback from the forming stars, their formation does not disrupt the group, although the stars and the gas may become separated due to the different forces on the two components (which is why it is important to model the stars as collisionless particles). Mergers and further accretion operate on the dynamical time and feed further star formation. Therefore, it is natural to expect the star formation rate to scale with the local dynamical time as our results demonstrate.

This explains the scaling but not the amplitude of relation shown in Figure 8. As we argued in § 4, this is too large because our effective efficiency for star formation is rather high (near unity integrated over many dynamical times, despite the low ϵ values adopted), again related to the longevity of the clusters. One possible reason behind the overproduction of stars is the lack of photoionization feedback from the newly formed stars. This will help in a number of ways, as the massive stars will quickly halt star formation in the rest of the cloud that has not collapsed, decreasing the efficiency in each cloud. It will also lead to the dispersal of the cloud, which will prevent mergers from producing clouds more massive than those observed. Indeed, in our simulations with Type II supernovae, these processes can be seen to operate, leading to a drop by a factor of 2–3 in the star formation rate for a given disk surface density. The timescale for photoionization is even shorter than the $\sim$10 Myr period before the first massive stars end their life and explode, which should lead to an even lower net efficiency.

We do not see clear large-scale spiral features in our simulated disks, perhaps indicating that the small-scale perturbations that we observe are insufficient to trigger low-m mode density waves. It remains to be seen if a more realistic simulation, including satellite perturbers, would be more successful at reproducing grand-design spiral features.

Recently, Li et al. (2005a, 2005b) have used SPH simulations of quiescent disks to argue that it is primarily the gravity that controls the star formation and gives rise to the Kennicutt relation between star formation and gas surface density. The results presented in this paper agree in the sense that gravity, rotation, and pressure naturally give rise to the observed slope of the Kennicutt relation, as well as a cutoff in the star formation rate beyond a certain radius. However, it is equally clear that some sort of feedback from the forming stars is required. The simulations of Li et al. (2005a, 2005b) used an isothermal equation of state and argued that an effective sound speed of approximately 10 km s^{-1} would match the observed star formation rates. They also adopted an efficiency of star formation in molecular clouds of 35%, again ascribing this to unmodeled feedback effects. Our simulations with supernova feedback do indeed reduce the star formation rate, and it is plausible that the addition of photoionization feedback would decrease this further. It is clear that further work is required.

One of the advantages of a more realistic equation of state is that we can naturally produce a multiphase ISM, with hot and cold phases existing in rough pressure equilibrium. A more detailed comparison with observations would be interesting, although a better heating and cooling model is probably required. In particular, we do not include a photo-heating source, which probably leads to an overestimate of the amount of cold, dense gas that can cool. Heating may reduce the star formation rate (although heating will be ineffective in the dense clumps that form from gravitational instabilities). The feedback also generates a galactic fountain, with star-forming regions ejecting gas out of the plane, which then falls back onto inactive regions.

Finally, we ask whether cosmological simulations adopting the C-type of star formation algorithm can realistically be used to model star-forming galactic disks. The answer appears to be a tentative yes, assuming that sufficiently high resolution is used to prevent spurious fragmentation in the stable part of the disk. As long as the correct parameters are chosen, we reproduce most of the features of the more realistic D-type model, in which stars form only in dense molecular clouds. The exception is the fraction of stars formed in bound clumps, which is lower in the C models than the D models. Models with supernova feedback reduce this discrepancy.

Although throughout this paper we have emphasized the similarities in the large-scale features between the C- and D-type models, the results are not identical. A more detailed study of the differences and their effects on the disk's structure and ISM will be a topic of future work.

7. CONCLUSIONS

We have performed high-resolution adaptive mesh refinement simulations of an isolated galactic disk evolved for more than 1 Gyr. We include many of the physical processes that must be important for the long-term evolution of the gas in spiral galaxies including cooling, shocks, self-gravity, star formation, and supernova feedback in a global three-dimensional model. Our adaptive mesh methodology allows us to resolve scales from 100 kpc down

to 25 pc, the size of typical giant molecular clouds. The physical model for the galactic disk is clearly oversimplified in a number of respects: it does not include magnetic fields, cosmic rays, or chemistry, and the cooling/heating model is incomplete. Still, this represents a substantial improvement over previous work in a number of ways (see § 1 for a discussion of previous simulation work) and represents some of the most realistic global disk simulations ever performed.

We performed a number of simulations while varying the input physics. This included runs with cooling down to two minimum temperatures (10^4 and 300 K), but no star formation. A series of runs were performed with cooling and two different prescriptions for star formation, the first a cosmological-simulation–inspired star formation algorithm that allowed star formation at relatively low densities but with a low efficiency, and the second a more physically minded algorithm that adopted a high-density threshold (comparable to that found in giant molecular clouds) before stars could form. These two forms we have denoted as C-type and D-type, respectively. We also performed some runs with spatial resolution 2 times better and mass resolution 8 times better in order to investigate numerical convergence. Finally, feedback from supernovae from massive stars was introduced.

Our results are summarized below:

1. Gravitational instabilities grow as long as the Toomre Q parameter is less than a critical value (0.6). Outside of this region, no stars form (although stars can be scattered into this region). This appears to be a well-resolved result and does not depend on the star formation algorithm.

2. If no star formation occurs, the clumps merge and form more massive, denser clouds. If star formation is permitted, stars form preferentially in the densest part of the clumps (particular for the D-type star formation algorithm). Without some form of feedback, the clouds are long-lived and convert a high fraction of their mass into stars.

3. Both star formation algorithms reproduce the slope of the observed relation between star formation and gas surface density. This appears to be because clump formation is controlled by the dynamical time. The C-type (cosmological) method can be tuned (with a sufficiently low efficiency parameter $\epsilon < 0.005$) to reproduce the observed normalization of the relation as well. The D-type method (with a high-density threshold) produces too many stars and will require some additional form of feedback to match the normalization. Energy input from Type II supernovae does indeed decrease the star formation rate (although more feedback, such as photoionization, seems to be required to match observations).

4. A multiphase ISM is naturally reproduced with most of the mass (>80%) in cold, dense clouds and peaks in the volume distribution at temperatures of approximately 10^4 and $10^{6.5}$ K.

5. Feedback from Type II supernovae drives material out of the plane of the disk (which then falls back). However, it does not increase the mean pressure in the plane of disk or generate large amounts of hot gas, or substantially increase the vertical scale height of the gas.

We thank Adrianne Slyz, Julien Devriendt, Yuexing Li, Mordecai Mac Low, Frazer Pearce, and the referee, Fabio Governato, for useful discussions. E. J. T. and G. L. B. acknowledge support from PPARC, and G. L. B. thanks the Leverhulme Trust. This work was partially supported by NSF grant AST 05-07161. Some simulations used in this paper were performed at the National Center for Supercomputing Applications.

REFERENCES

Boissier, S., Prantzos, N., Boselli, A., & Gavazzi, G. 2003, MNRAS, 346, 1215
Boulares, A., & Cox, D. P. 1990, ApJ, 365, 544
Bryan, G. L. 1999, Comput. Sci. Eng., 1, 46
Bryan, G. L., & Norman, M. L. 1997, in ASP Conf. Ser. 123, Computational Astrophysics: 12th Kingston Meeting on Theoretical Astrophysics, ed. D. A. Clarke & M. J. West (San Francisco: ASP), 363
Bryan, G. L., Norman, M. L., & Abel, T. 2001, preprint (astro-ph/0112089)
Cen, R., & Ostriker, J. P. 1992, ApJ, 399, L113
Chu, Y. 1999, Ap&SS, 269, 441
de Avillez, M. A. 2000, MNRAS, 315, 479
Elmegreen, B. G., Kim, S., & Staveley-Smith, L. 2001, ApJ, 548, 749
Ferguson, A. M. N., Wyse, R. F. G., & Gallagher, J. S. 1996, AJ, 112, 2567
Gammie, C. F. 2001, ApJ, 553, 174
Goldreich, P., & Lynden-Bell, D. 1965, MNRAS, 130, 97
Heyer, M. H., Corbelli, E., Schneider, S. E., & Young, J. S. 2004, ApJ, 602, 723
Jenkins, E. B. 1978, ApJ, 220, 107
Kennicutt, R. C., Jr. 1989, ApJ, 344, 685
———. 1998, ApJ, 498, 541
Kim, W.-T., & Ostriker, E. C. 2001, ApJ, 559, 70
Kim, W.-T., Ostriker, E. C., & Stone, J. M. 2003, ApJ, 599, 1157
Klypin, A., Zhao, H., & Somerville, R. S. 2002, ApJ, 573, 597
Korpi, M. J., Brandenburg, A., Shukurov, A., Tuominen, I., & Nordlund, Å. 1999, ApJ, 514, L99
Kravtsov, A. V. 2003, ApJ, 590, L1
Kritsuk, A., & Norman, M. L. 2002, ApJ, 569, 127L
Lada, C. J., & Lada, E. A. 2003, ARA&A, 41, 57
Larson, R. B. 1981, MNRAS, 194, 809
Li, Y., Mac Low, M.-M., & Klessen, R. 2005a, ApJ, 620, 19L
———. 2005b, ApJ, 626, 823
Mac Low, M.-M., & Klessen, R. S. 2004, Rev. Mod. Phys., 76, 125
Malhotra, S. 1995, ApJ, 448, 138
Marri, S., & White, S. D. M. 2003, MNRAS, 345, 561
Martin, C. L., & Kennicutt, R. C., Jr. 2001, ApJ, 555, 301
McCray, R., & Snow, T. P. 1979, ARA&A, 17, 213
McKee, C. F., & Ostriker, J. P. 1977, ApJ, 218, 148
Navarro, J., Frenk, C., & White, S. D. M. 1997, ApJ, 490, 493
Norman, M. L., & Bryan, G. L. 1999, in Numerical Astrophysics, ed. S. M. Miyama, K. Tomisaka, & T. Hanawa (Boston: Kluwer), 19
O'Shea, B. W., Bryan, G., Bordner, J., Norman, M. L., Abel, T., Harkness, R., & Kritsuk, A. 2004, preprint (astro-ph/0403044)
Rafikov, R. R. 2001, MNRAS, 323, 445
Robertson, B., Yoshida, N., Springel, V., & Hernquist, L. 2004, ApJ, 606, 32
Rosen, A., & Bregman, J. N. 1995, ApJ, 440, 634
Sarazin, C. L., & White, R. E. 1987, ApJ, 320, 32
Schmidt, M. 1959, ApJ, 129, 243
Sellwood, J. A., & Balbus, S. A. 1999, ApJ, 511, 660
Semelin, B., & Combes, F. 2002, A&A, 388, 826
Shelton, R. L., & Cox, D. P. 1994, ApJ, 434, 599
Shelton, R. L., et al. 2001, ApJ, 560, 730
Slyz, A. D., Devriendt, J. E. G., Bryan, G., & Silk, J. 2005, MNRAS, 356, 737
Springel, V., & Hernquist, L. 2003, MNRAS, 339, 289
Stanimirovic, S., Staveley-Smith, L., Dickey, J. M., Sault, R. J., & Snowden, S. L. 1999, MNRAS, 302, 417
Stone, J. M., & Norman, M. L. 1992, ApJS, 80, 753
Toomre, A. 1964, ApJ, 139, 1217
Truelove, J. K., Klein, R. I., McKee, C. F., Holliman, J. H., Howell, L. H., & Greenough, J. A. 1997, ApJ, 489, L179
Wada, K. 2001, ApJ, 559, L41
Wada, K., Meurer, G., & Norman, C. A. 2002, ApJ, 577, 197
Wada, K., & Norman, C. A. 2001, ApJ, 547, 172
Wolfire, M. G., McKee, C. F., Hollenbach, D., & Tielens, A. G. G. M. 2003, ApJ, 587, 278